



An Investigation of the Aerodynamics of a Harmonically-Pitching Airfoil in Uniform-Shear Approach Flow

Patrick R. Hammer¹, David A. Olson²,
Michigan State University, East Lansing, MI, 48824

Miguel R. Visbal³
U.S. Air Force Research Laboratory, Wright-Patterson Air Force Base, Dayton, OH, 45433

and

Ahmed M. Naguib⁴ and Manoochehr M. Koochesfahani⁵
Michigan State University, East Lansing, MI, 48824

This work explores the aerodynamics of an airfoil oscillating in a uniform shear flow at chord-Reynolds number of approximately 1.2×10^4 using complementary two-dimensional Navier-Stokes computations and direct force measurements. A NACA 0012 airfoil is pitched harmonically about its quarter-chord, with 2° amplitude and reduced frequency up to 12, in positive-shear approach flow for non-dimensional shear values in the range 0.0 – 1.0. Previous steady airfoil results showed the development of negative lift at zero angle of attack in the presence of positive shear, *opposite of the inviscid theory*, and symmetry breaking in the wake. The negative lift magnitude and symmetry breaking in the wake increased with the non-dimensional shear rate. In the current results for an *unsteady* airfoil, the wake also exhibits symmetry breaking that leads to a deflected wake towards the high-speed side as the reduced frequency increases beyond the reduced frequency for an aligned vortex street. Interestingly, the presence of shear seems to have little or no effect on the average thrust and peak-to-peak lift and thrust fluctuation, while a prominent influence is seen on the average lift. The latter switches sign from negative to positive at a reduced frequency of approximately 3, and it increases in magnitude with both increasing non-dimensional shear rate and reduced frequency.

I. Introduction

An extensive body of work exists on the unsteady aerodynamics of oscillating airfoils (e.g. [1-9]). Whether the oscillatory motion is in the form of pitch, plunge (heave), or a combination of both, the focus has been almost exclusively on uniform freestream conditions. There are many situations of engineering interest in which aircraft encounter non-uniform (shear) approach flows. These situations include wings near the ground, wind shear, ambient wind conditions that are altered by large scale disturbances (e.g. mountains), and aircraft operating in close proximity, among others. Understanding the unsteady forces acting on an oscillating airfoil in such situations is significant for predicting and controlling the aeroelastic behavior of airfoils; such as that associated with flutter vibrations.

The overarching objective of the present study is to develop an integrated computational-experimental framework for the study of the aerodynamics of unsteady airfoils in an approach stream exhibiting prescribed non-uniformities.

¹ Post-Doctoral Researcher, Mechanical Engineering, 1449 Engineering Research Ct A108, East Lansing, MI 48824, AIAA Member.

² Graduate Student, Mechanical Engineering, 1449 Engineering Research Ct A109, East Lansing, MI 48824, AIAA Member.

³ CFD Technical Advisor, Air Force Research Laboratory, Wright-Patterson Air Force Base, OH 45433, AIAA Fellow.

⁴ Professor, Mechanical Engineering, 1449 Engineering Research Ct C128, East Lansing, MI 48824, AIAA Associate Fellow.

⁵ Professor, Mechanical Engineering, 1449 Engineering Research Ct A131, East Lansing, MI 48824, AIAA Associate Fellow.

In this paper, we report on the progress towards this goal by focusing on the specific case of small-amplitude, high-frequency, harmonically pitching airfoils placed in a uniform-shear freestream (i.e., where the velocity varies linearly with the cross-stream coordinate). As depicted in Fig. 1, the shear zone is parameterized by its thickness δ and velocity gradient, or shear rate, dU/dy . The corresponding non-dimensional parameters are δc and $\gamma = (dU/dy) \times (c/U_o)$; where c is the chord length and U_o is a reference velocity, defined as that of the approach stream at the cross-stream coordinate y of the pitch axis. Both computational and experimental efforts are reported with the goal of investigating the unsteady forces acting on the airfoil and their physical connection(s) to the flow features.

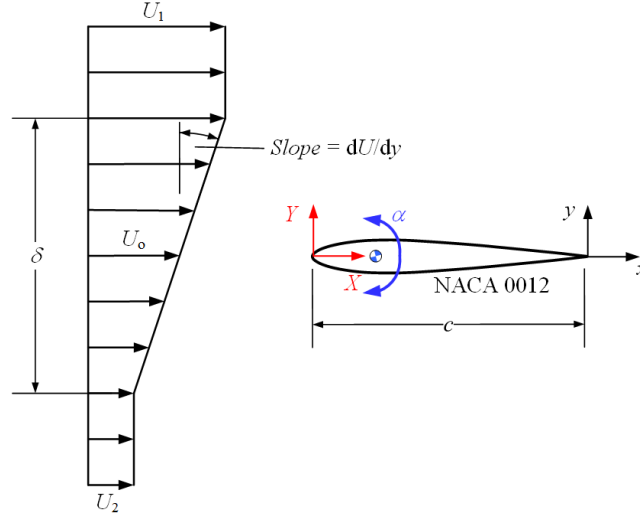


Figure 1. Schematic of the flow configuration depicting a three-segment approach stream with a central uniform-shear segment having thickness δ and bounded by high- and low-speed uniform streams with velocities U_1 and U_2 respectively. Two coordinate systems are defined: (X, Y) with origin at the leading edge, and (x, y) with origin at the trailing edge, when the airfoil is at zero angle of attack.

II. Computational Details

A. Numerical Method

The computations are performed using the high-order, extensively validated FDL3DI solver [10, 11], which solves the full, compressible, unsteady, three-dimensional Navier-Stokes equations. Here, the code is run to perform two-dimensional simulations. Upon transforming the Cartesian coordinate system (x, y, t) to a curvilinear coordinate system (ξ, η, τ) , the governing equations are written in strong conservative form, resulting in the following:

$$\frac{\partial}{\partial \tau} \left(\frac{\vec{Q}}{J} \right) + \frac{\partial \hat{F}_I}{\partial \xi} + \frac{\partial \hat{G}_I}{\partial \eta} = \frac{1}{Re_c} \left[\frac{\partial \hat{F}_V}{\partial \xi} + \frac{\partial \hat{G}_V}{\partial \eta} \right] \quad (1)$$

In Eq. (1), $\vec{Q} = [\rho, \rho u, \rho v, \rho E]^T$ is the solution vector, J is the transformation Jacobian, \hat{F}_I and \hat{G}_I are the inviscid fluxes, and \hat{F}_V and \hat{G}_V are the viscous fluxes (refer to reference [12] for further details on these quantities). The two-dimensional Cartesian velocity components are u and v , ρ is the density, and p is the pressure. The ideal gas law and Sutherland's law for viscosity are also assumed to complete the set of equations. All flow variables have been normalized by their reference centerline values, except for pressure, which has been non-dimensionalized by $\rho_o U_o^2$, where ρ_o and U_o represent the centerline, reference values.

Time accurate solutions of Eq. (1) are obtained numerically using the implicit, approximately-factored method developed by Beam and Warming [13]. This expression had been simplified through the diagonalization of Pulliam and Chaussee [14] and supplemented with Newton-like subiterations to achieve second-order accuracy. In "delta" form, this algorithm is given by:

$$\begin{aligned}
& \left[\left(\frac{1}{J} \right)^{p+1} + \varphi^i \Delta \tau \delta_{\xi,2} \left(\frac{\partial \hat{F}_i^p}{\partial \bar{Q}} - \frac{1}{Re_c} \frac{\partial \hat{F}_v^p}{\partial \bar{Q}} \right) \right] J^{p+1} \\
& \times \left[\left(\frac{1}{J} \right)^{p+1} + \varphi^i \Delta \tau \delta_{\eta,2} \left(\frac{\partial \hat{G}_i^p}{\partial \bar{Q}} - \frac{1}{Re_c} \frac{\partial \hat{G}_v^p}{\partial \bar{Q}} \right) \right] \Delta \bar{Q} \\
& = -\varphi^i \Delta \tau \left[\left(\frac{1}{J} \right)^{p+1} \frac{(1+\varphi)\bar{Q}^p - (1+2\varphi)\bar{Q}^n + \varphi\bar{Q}^{n-1}}{\Delta \tau} + \bar{Q}^p \left(\frac{1}{J} \right)_\tau^p \right. \\
& \quad \left. + \delta_{\xi,6} \left(\hat{F}_i^p - \frac{1}{Re_c} \hat{F}_v^p \right) + \delta_{\eta,6} \left(\hat{G}_i^p - \frac{1}{Re_c} \hat{G}_v^p \right) \right]
\end{aligned} \tag{2}$$

where $\varphi = 1/2$ yields second-order accurate algorithm, $\varphi^i = 1/(1+\varphi)$, and $\Delta \bar{Q} = \bar{Q}^{p+1} - \bar{Q}^p$. At the first subiteration level ($p=1$), $\bar{Q}^p = \bar{Q}^n$, where \bar{Q}^p is the subiteration approximation of \bar{Q}^{n+1} . As the number of subiterations increases, \bar{Q}^p approaches \bar{Q}^{n+1} . The use of subiterations allows for the elimination of errors due to the linearization, factorization, diagonalization, etc. On the unknown left-hand-side of Eq. (2), spatial derivatives are calculated using a second-order central difference scheme. Fourth-order, nonlinear artificial dissipation terms are added to augment stability in the left-hand side [15, 16], but these are not shown in Eq. (2).

On the right-hand side of Eq. (2), a sixth-order compact finite difference scheme [17] is employed to discretize the governing equations. For any scalar quantity, ϕ , such as a metric, flux component, or flow variable, the spatial derivative, ϕ' , is obtained along a coordinate line in the computational domain by solving the tridiagonal system:

$$\psi \phi'_{i-1} + \phi'_i + \psi \phi'_{i+1} = a \frac{\phi_{i+1} + \phi_{i-1}}{2} + b \frac{\phi_{i+2} + \phi_{i-2}}{4} \tag{3}$$

High-order formulas that retain the tridiagonal form are used at the boundaries. To eliminate spurious frequency components, a high-order Padé-type low-pass spatial filter [10] is used. The filtered value of a component in the solution vector, $\hat{\phi}_i$, is computed with the following tridiagonal system:

$$\psi_f \hat{\phi}_{i-1} + \hat{\phi}_i + \psi_f \hat{\phi}_{i+1} = \sum_{n=0}^N \frac{a_n}{2} (\phi_{i+n} + \phi_{i-n}) \tag{4}$$

With the proper choice of coefficients, the formula provides a $2N$ th-order filter on a $2N+1$ point stencil. For this work, an 8th-order filter is used for the interior points. Near the boundary, filtering strategies used by [11] are implemented. The filter is applied to the conserved variables along each coordinate direction once per time-step and subiteration. For additional details on the computations and validation based on a uniform approach flow, see reference [18].

B. Flow and Computational Parameters

The computations are performed on a NACA 0012 airfoil with a rounded trailing edge ($r_{TE} = 2.2 \times 10^{-3}c$). An overset computational grid is used for this work (see Fig. 2). An O-grid (Fig. 2a) wraps around the airfoil with dimensions 655×165 , leading-edge spacing $\Delta \xi_{LE} = 5.0 \times 10^{-4}c$, trailing-edge spacing $\Delta \xi_{TE} = 2.5 \times 10^{-4}c$, and initial normal spacing at the wall $\Delta \eta_{wall} = 5.0 \times 10^{-5}c$. A single Cartesian background grid is used to maintain the shear profile in the approach stream while resolving the wake structure with high spatial resolution (Fig. 2b). Holes are cut in the background grid to blank out the region of the background grid coincident with the O-grid using NASA code Pegasus 5 [19]. The high-resolution wake region covers four chord lengths downstream of the trailing edge in the streamwise direction and 1.8 chord lengths in the transverse direction with uniform spacing of $2.5 \times 10^{-3}c$. The Cartesian grid is then rapidly stretched to over 100 chords (Fig. 2c). This stretching along with the high-order filter helps eliminate spurious reflections off the boundary [20]. Grid communication and low-order interpolation are performed as a pre-processing step using Pegasus 5 [19], which are then extended to high-order [21, 22].

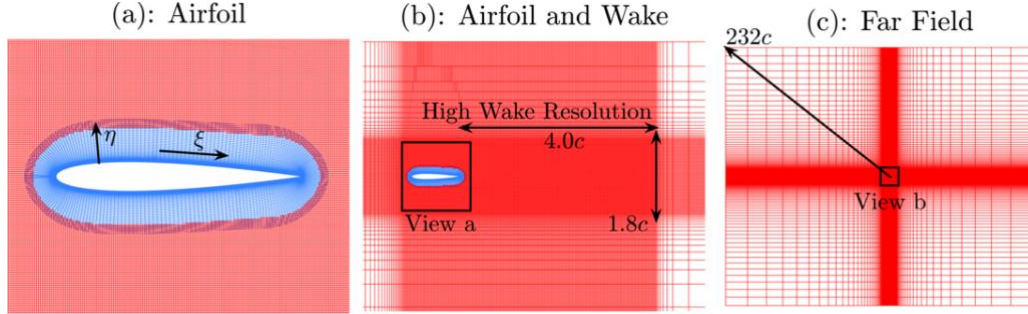


Figure 2. Schematic of the computational domain, showing three fields of view with varying degrees of enlargement. In views (a) and (b), grid points have been removed for clarity.

The boundary conditions are prescribed as follows. A no-slip, adiabatic condition is applied at the wall in conjunction with a zero-normal pressure gradient. The three-segment streamwise velocity profile (shown in Fig. 1), uniform static pressure, and uniform total temperature conditions are specified along the upstream far-field boundary. At the three additional far-field boundaries, a first-order accurate extrapolation condition is applied to the primitive variables, except for pressure, which is uniform. Spatial periodicity is enforced in the azimuthal direction of the O-grid using a five-point overlap. The computation is initialized using the converged solution for the steady airfoil at zero angle of attack.

The Reynolds number of the computations is 1.2×10^4 based on the chord length, c , and the reference velocity, U_o . For the present work, the pitch axis at the quarter-chord is placed at the center of the shear zone. The non-dimensional shear rate $\dot{\gamma}$ varies from 0.0 (uniform flow) to 1.0, and the shear zone width δ is set to $1.5c$. This value is selected to be large enough such that the results are nearly independent of δ ; i.e. equivalent of placing the airfoil in an infinitely wide shear zone. The reduced frequency, $k = \pi f c / U_o$, where f is the oscillation frequency, varies from 0 to approximately 12. The pitching amplitude α_o is 2° , with pitching done about the quarter-chord from the leading edge, resulting in a maximum Strouhal number based on trailing edge amplitude, $St = k A_{TE} / c \pi$, of 0.2. Sinusoidal oscillations are utilized around a zero mean angle of attack for all simulations.

The solution advances in time with a computational time-step, $\Delta \tau = \Delta t U_o / c$, of 5.0×10^{-5} in conjunction with *seven* subiterations per time-step. To simulate the incompressible limit with the current compressible solver, a low reference Mach number, M_o , of 0.015 is used. Justification for the selection of these parameters is based on previous studies in uniform flow [18] and have been verified for the case of a shear approach flow.

Simulations are carried out for 15 to 70 oscillation cycles, at which point the change in average lift and thrust coefficients converge to better than 1%. Ninety-six instantaneous phases spanning one oscillation cycle are then extracted from the simulation and wake data from both the airfoil grid and the background grid are remapped onto a Cartesian grid with uniform spacing of $2.5 \times 10^{-3} c$ for computing the time-average and *rms* of the streamwise (u) and cross-stream (v) velocity components.

C. Grid Deformation

Since the upstream boundary condition is spatially varying in the cross-stream direction, the overset grid is dynamically deformed, instead of rigidly rotated, to accommodate the sinusoidal pitching motion instead of rigidly rotated. The deforming grid strategies employed in [23-25] are used. First, two circles of diameters D_1 and D_2 are created in the domain centered about the pitching axis. All grid points within D_1 define a region in which the grid rigidly rotates (Region 1) while grid points outside of D_2 remain stationary (Region 3). The remaining grid points (Region 2) deform smoothly according to Eq. (5), where the blending function is defined as $\beta = 10r^3 - 15r^4 - 6r^5$:

$$\vec{x}_d = \beta \vec{x}_{ud} + (1 - \beta) \Delta \vec{x}_{rig} \quad (5)$$

In Eq. (5), \vec{x}_{ud} is the position vector of the un-deformed grid points, \vec{x}_d is the position vector of the deformed grid points, $\Delta \vec{x}_{rig}$ is the displacement vector due to rigid-body motion. Note that $\beta = 0$ for grid points in Region 1 and $\beta = 1$ for grid points in Region 3. Although no issues related to the size of the deforming zone (and hence far-field grid resolution) are observed for the uniform flow case, numerical artifacts are seen in the shear case when the deforming zone encompasses grid points being stretched to the far field. By using $D_1 = 2c$ and $D_2 = 10c$, the deforming zone remains close to the airfoil and does not distort the approach velocity profile.

III. Experimental Details

The experiments are conducted in a closed-return 61 cm \times 61 cm free-surface water tunnel at the Turbulent Mixing and Unsteady Aerodynamics Laboratory (TMUAL) at Michigan State University. The tunnel is fitted with a three-degree-of-freedom (3DOF) servo motion system that is capable of producing pitch, heave and surge motion. Only the pitch motion is utilized in the present work. A NACA 0012 airfoil with 12 cm chord length and aspect ratio $AR = 5.14$ is attached to the pitch axis via a force balance, as depicted in Fig. 3. The shaft connecting the airfoil to the balance, passes through a “skimmer plate” (not shown in Fig. 3), which skims the water free surface and spans the full test-section width to avoid disturbing the free surface during airfoil oscillation, and to provide a well-defined boundary condition on the top side of the airfoil. Less than a 0.5 mm clearance gap is left between the top end of the airfoil and the skimmer plate, on one hand, and the bottom end of the airfoil and the test section floor, on the other. The pitch motor is fitted with high-resolution encoder that captures the airfoil pitch angle with high resolution: 0.003 degrees.

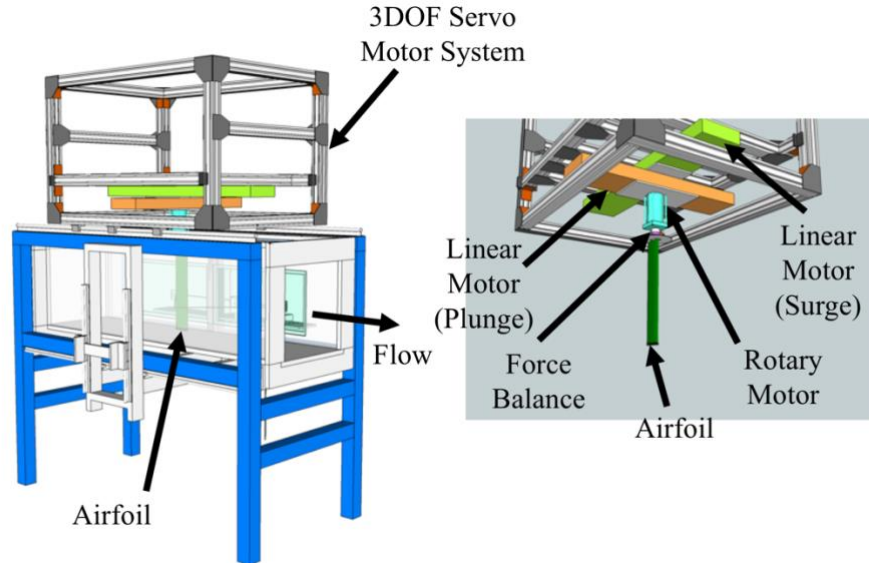


Figure 3. 3D model of the water tunnel test section, depicting the vertical airfoil mounted to the 3DOF motion system on top of the test section (left). Details of the 3DOF system and airfoil mounting (right).

To generate shear in the freestream, the shaped honeycomb technique of [26], with some additional refinements [27], is used. The desired cross-stream velocity variation downstream of the honeycomb is prescribed and the honeycomb profile shape required to produce this variation is computed for a 61 cm wide, 3.175 mm cell-diameter honeycomb structure. The device is inserted in the path of the uniform flow entering the test section (see Fig. 4) in order to produce variable flow resistance, and hence generate variation in the velocity in the cross-stream direction. For the present measurements, a three-segment profile with a central uniform-shear zone having $\dot{\gamma} = 0.5$ and $\delta/c = 2.0$ is targeted. The actual velocity profile produced by the honeycomb is measured using molecular tagging velocimetry and the results are displayed in Fig. 5. In comparison to the target velocity profile (also shown in Fig. 5), the actual velocity variation exhibits an undershoot where the shear zone meets the low-speed stream, a rather small overshoot on the high-speed side, and the overall velocity difference across the shear ($\Delta U = U_1 - U_2$) is less than intended. However, a fairly sizable central zone with linear velocity variation (uniform shear) is observed. The uniform-shear zone width is approximately $1.7c$ and the shear rate $\dot{\gamma} = 0.48$.

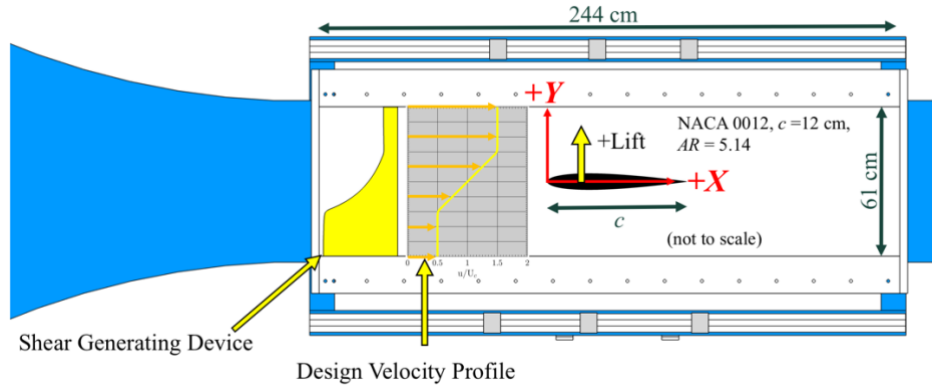


Figure 4. Top view of the test section showing placement of the honeycomb shear generator, a schematic of the approach stream velocity profile and the NACA 0012 airfoil.

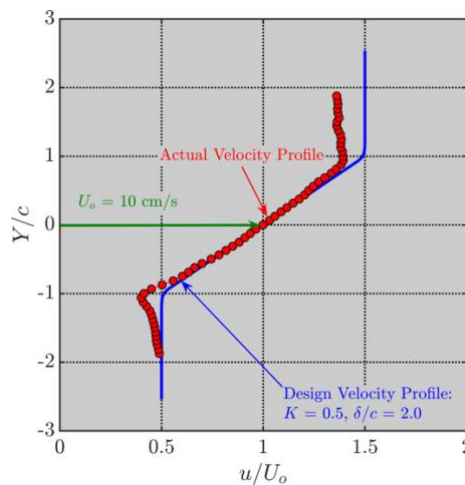


Figure 5. Measured streamwise velocity profile of the approach stream (red symbols), with the target profile (blue line) shown for reference. The experimental profile is measured without the airfoil in the flow where the leading edge would be.

Load measurements are carried out using an ATI Mini40 six-component force balance/load cell. Only the lift and drag force components are measured in the present study. To account for the inertia forces produced during oscillatory pitching due to the mass of the airfoil, support shaft, and other components mounted on the pitch axis, force measurements are conducted with the airfoil placed in still air while executing the same pitch oscillations as used in the water tunnel tests. Results from these measurements are found to be negligible (primarily due to the axially aligned center of mass of all sub-components) and are therefore, not utilized in this study. Also, “flow-off” measurements of forces are conducted in the water tunnel immediately preceding and following the “flow-on” measurements. The duration of each experiment is kept to less than 15 minutes such that load cell drift is also negligibly small (less than the resolution reported below). The resolution, based on sensor specifications, of lift/drag force measurements is 0.005 N for the Mini 40. The corresponding lift/drag coefficient resolution is 0.014. The uncertainty of the mean force coefficient measurements for the static airfoil tests is estimated to be 0.005 based on the standard error of the mean and accounting for drift over the duration of each measurement.

Zero angle of attack is determined from force measurements versus angle of attack for the static airfoil in uniform approach stream. The angle at which the total measured sectional force vector magnitude is minimum is taken as $\alpha_m = 0^\circ$. In addition, possible small misalignment between the force axes of the load cell and the flow coordinates is accounted for iteratively by checking the symmetry of the lift and drag measurements with respect to $\alpha_m = 0^\circ$. For all cases, the airfoil is pitched harmonically around the quarter-chord point. The oscillations have a fixed amplitude of 2° and the airfoil oscillates with several reduced frequencies extending from $k = 0.0$ (no oscillation) to $k = 6.0$. The reference velocity U_o is set to 10 cm/s, yielding a chord Reynolds number $Re_c = 1.25 \times 10^4$, which is close to the Reynolds number in the computations.

IV. Results

A. Aerodynamic Characteristics of a Steady Airfoil in Shear

Before considering the unsteady airfoil, it is of interest to demonstrate the effect of shear on the aerodynamic characteristics (i.e., loads and wake structure) for the baseline, steady airfoil. According to Tsien's inviscid theory for a Joukowski airfoil [28], the lift at zero angle of attack has the same sign as the approach-stream shear (i.e., the lift is positive in positive shear) and increases in magnitude as the shear rate increases. This results in an upward shift of the lift curve, and hence a negative shift of the zero-lift angle of attack. Fig. 6a shows the average lift coefficient C_L against the non-dimensional shear rate for the steady NACA 0012 airfoil at zero angle of attack for both the viscous flow at $Re_c = 1.2 \times 10^4$ and the corresponding inviscid solution.

As seen in Fig. 6a, the C_L magnitude increases with the shear rate while having a negative sign; *opposite to that predicted by inviscid theory!* The inviscid solution, also shown in Fig. 6a, is computed using a panel method that has been validated against Tsien's theory for Joukowski airfoil [25]; see the comparison between the yellow triangles and the black line in Fig. 6a. The explanation for the qualitatively opposite trends of the viscous and inviscid solutions is linked to the breaking of symmetry in the boundary layer evolution between the top and the bottom surfaces of the airfoil. This asymmetry is significant at sufficiently low Reynolds number to produce an *apparent* airfoil shape with negative camber. These details are the subject of a separate article [29]. Figure 6b shows experimental data of C_L against mean angle of attack for uniform and shear approach flow. For comparison, the figure also contains a few CFD data points, which are computed by prescribing the upstream boundary condition to be the same as the measured experimental velocity profile; specifically, a spline fit to the red symbols in Fig. 5. Both the CFD and the experimental data show shear in the approach flow shifts the zero-lift angle of attack to a positive value. Equivalently, the two approaches depict negative C_L at zero angle of attack.

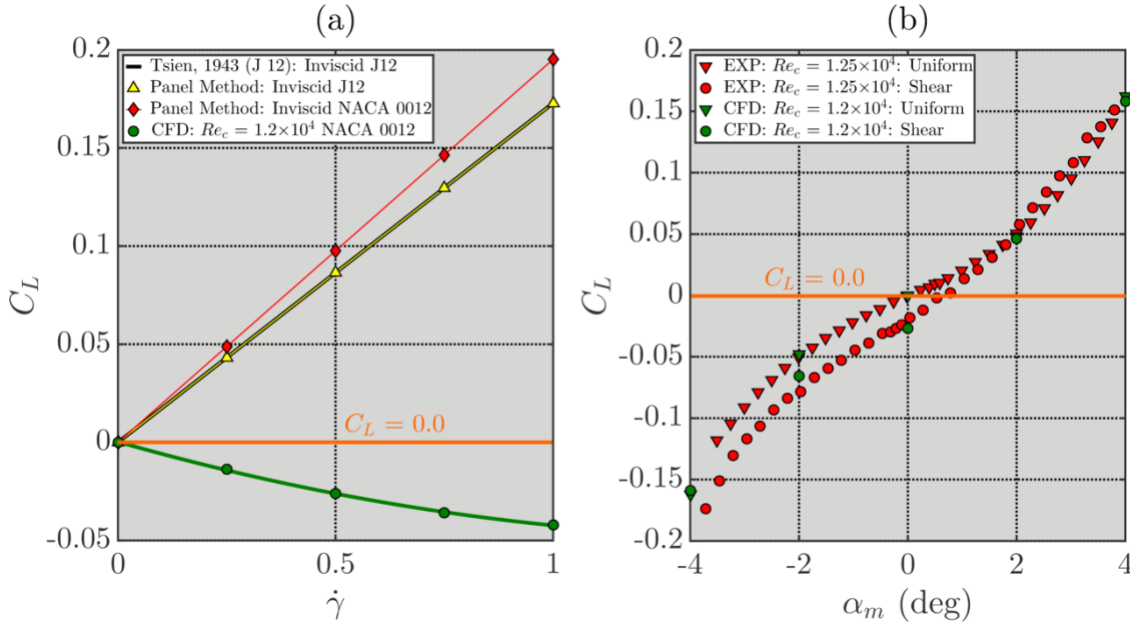


Figure 6. (a) Average lift coefficient vs. shear rate and (b) angle of attack for a steady airfoil at zero angle of attack. In the left plot, two inviscid-flow cases are included: one based on Tsien's theoretical solution for 12%-thick Joukowski (J12) airfoil [25], and the other using a panel method for J12 and NACA 0012 airfoils. The comparison of the J12 results from Tsien's theory and the present panel method is used to validate the panel method. The CFD solver is FDL3DI [10, 11]. The data in the right plot, where "Shear" corresponds to $\dot{\gamma} = 0.48$, include CFD results obtained using the same approach stream velocity profile as in the experiments (depicted in Fig. 5).

The influence of shear on the baseline wake structure is visualized in Fig. 7 using instantaneous spanwise vorticity (ω_z) fields. In uniform flow ($\dot{\gamma} = 0.0$), the shear layer coming off the airfoil trailing edge goes unstable and rolls up into a classical von Kármán vortex street. In shear, the wake structure becomes asymmetric. At $\dot{\gamma} = 0.5$, the negative vorticity in the wake, which has the same sign as the approach stream's vorticity, becomes slightly higher while the positive vorticity diminishes. This asymmetry becomes more obvious as the shear rate increases to $\dot{\gamma} = 1.0$.

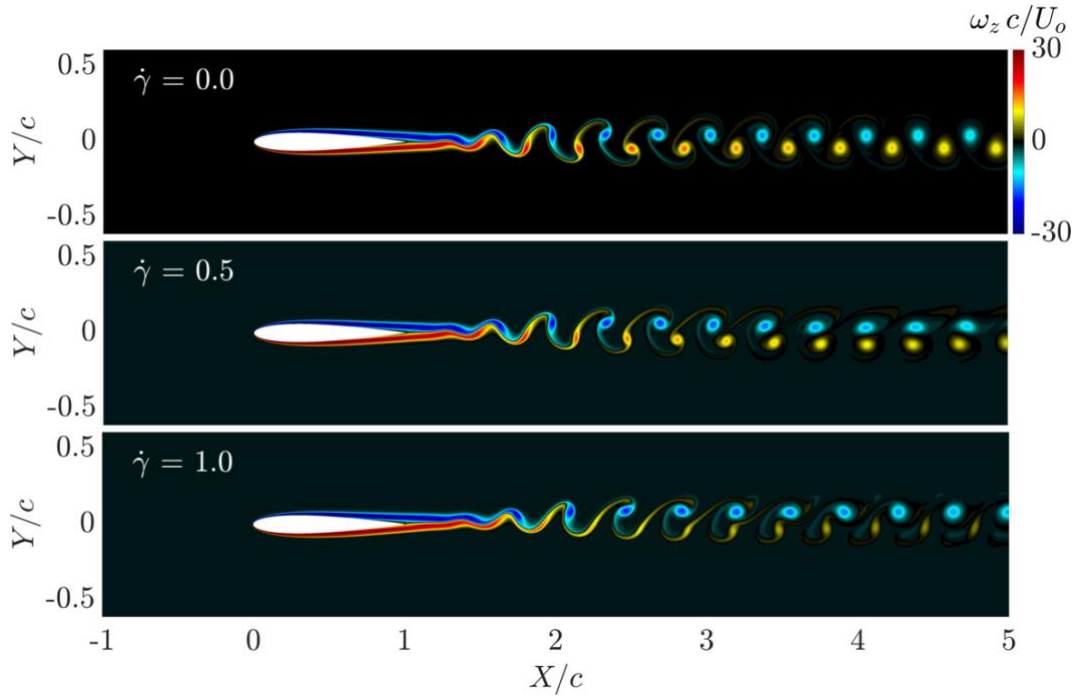


Figure 7. Instantaneous spanwise vorticity fields for different non-dimensional shear rates, with increasing shear rate from top to bottom. The airfoil is steady and at zero angle of attack.

B. Unsteady Airfoil

1. Wake Characteristics

Figure 8 displays cross-stream profiles of the average u and v velocity components in the wake of the airfoil in uniform stream (i.e., $\dot{\gamma} = 0.0$) for different reduced frequencies, while Fig. 9 shows the corresponding rms velocity profiles. The profiles are extracted one chord length downstream of the trailing edge ($x/c = 1.0$). A few observations can be made, which are consistent with the well documented behavior of the wake of pitching airfoils in uniform flow; e.g. [1] and [8]. When the airfoil is steady (i.e., $k = 0.0$), there is a clear wake deficit consistent with the arrangement of the vortices in the von Kármán vortex street pattern (Fig. 7, top plot). At $k = 5.2$, the u_{avg} profile maintains a deficit in velocity, suggesting the persistence of the Kármán vortex street pattern, as well as an over-shoot in velocity. At $k = 6.0$, the u_{avg} profile shows a *slight* jet, implying that the wake structure has flipped to a reverse von Kármán street pattern. As the reduced frequency increases further, the profile maintains the jet-like character with the magnitude of the centerline velocity increasing with frequency. The average v profile remains nearly zero across the wake for all cases. The profiles of the streamwise and cross-stream velocity fluctuations exhibit one or more local peaks. The locations of these peaks can be readily connected to the wake vortex configuration. The sharp drop in centerline u_{rms} for $k = 6.0$ indicates the vortices are nearly aligned along the wake centerline when the wake switches over from the traditional to the reverse von Kármán street pattern; the so-called “neutral” wake. These features are well understood and have previously been replicated using a low-order vortex array model [29].

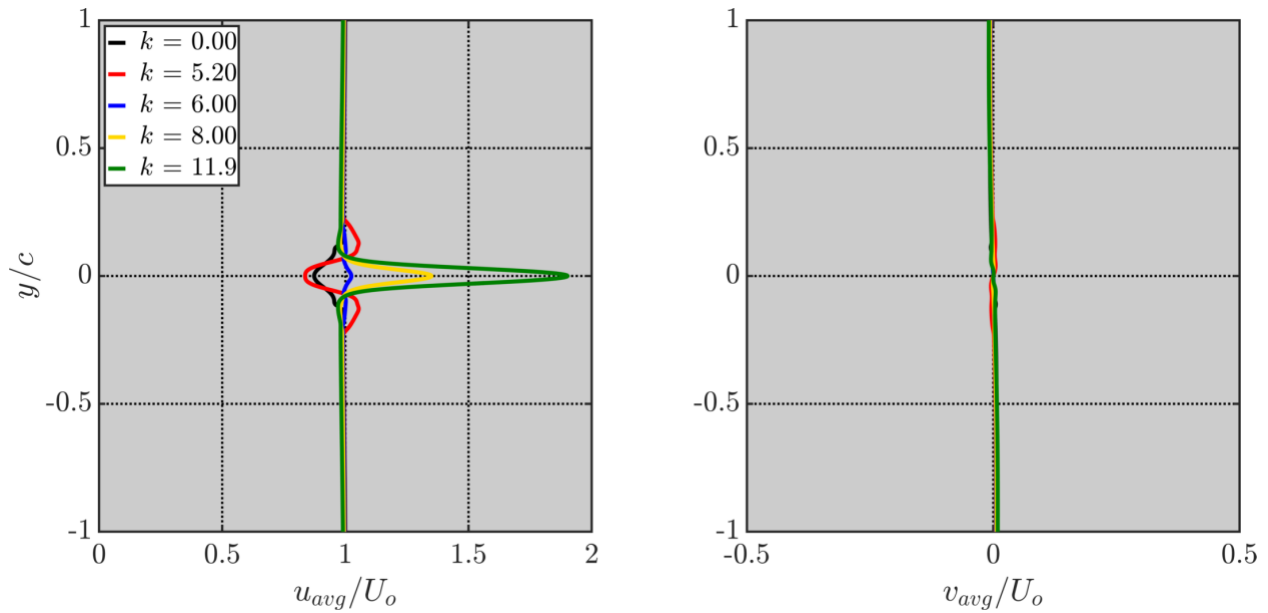


Figure 8. Cross-stream profiles of the average streamwise and cross-stream velocity, extracted at $x/c = 1.0$ for different values of the reduced frequency. The approach flow is uniform ($\dot{\gamma} = 0.0$).

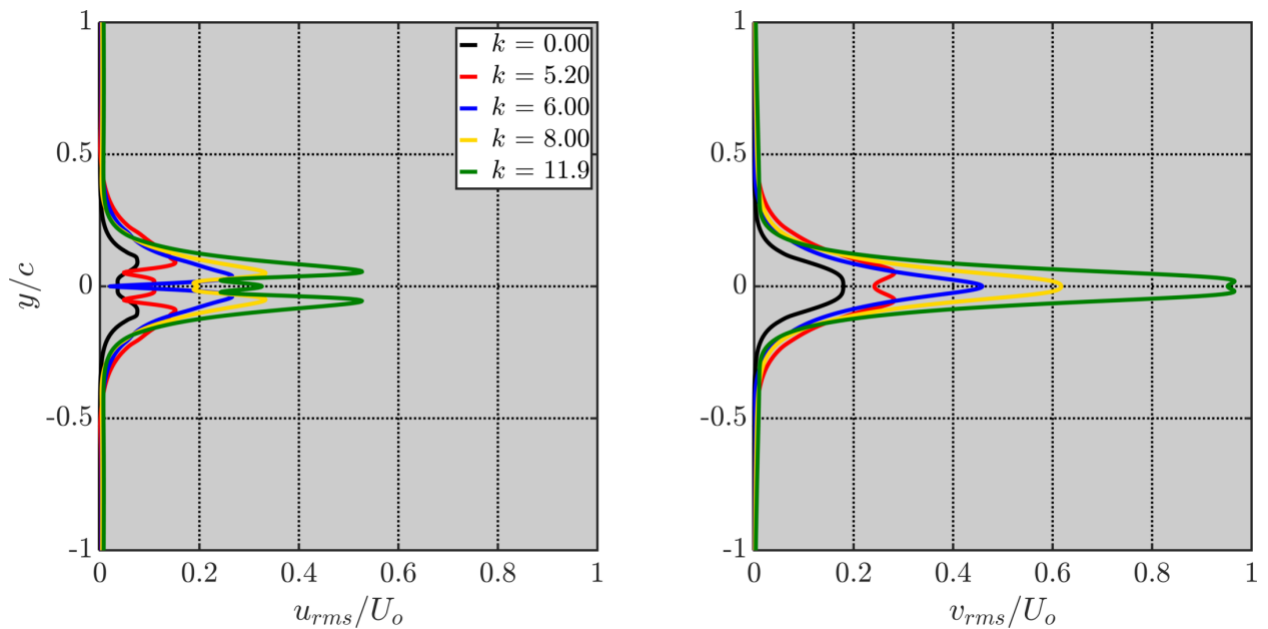


Figure 9. Cross-stream profiles of the *rms* streamwise and cross-stream velocity, extracted at $x/c = 1.0$ for different values of the reduced frequency. The approach flow is uniform ($\dot{\gamma} = 0.0$).

Figures 10 and 11 provide the average and the *rms* profiles, respectively, of u and v for different reduced frequencies, extracted at the same location as the profiles in Fig. 8 and 9 ($x/c = 1.0$) for the highest shear rate considered, $\dot{\gamma} = 1.0$. The most obvious feature of the u_{avg} profiles that is distinctly different from the uniform-flow case is that they have an overall shape similar to that of the three-segment uniform shear profile of the approach stream “superposed” on the wake disturbance. This disturbance, or deviation from the shear profile, bears some similarities with the profiles for the uniform flow case. Specifically, at $k = 0.0$ and 5.2 , the disturbance exhibits a deficit in velocity, while a jet-like flow is established over part of the wake at $k = 8.0$ and 11.9 . At $k = 6.0$, the three-segment shear profile is almost undisturbed by the presence of the wake, suggesting the alignment of the wake vortices with the wake centerline. Thus, interestingly, it appears that the neutral wake is established at the same reduced frequency for both

the uniform and shear flow cases; unaffected by the presence of shear. Further confirmation of this conclusion will be seen when considering the wake flow structure below.

Notwithstanding the noted similarities, there are a few differences between the u_{avg} profiles of the uniform and shear flow. For $k > 6.0$, the maximum velocity in the jet progressively shifts in the positive y direction with increasing k , suggesting the wake deflects to the high-speed-side. Moreover, the deviation from the overall three-segment uniform shear profile is not jet-like for the entire width of the wake, as predominantly the case for uniform flow. A fairly substantial region of wake-like behavior is seen below the jet. The cross-stream width and deficit magnitude of this region increase with the reduced frequency. A similar combination of velocity deficit and excess is also seen at $k = 5.2$, where the wake-deficit is the dominant part. The v -component of velocity also shows behavior that deviates from that observed for the uniform flow case. For $k \leq 6.0$, the average- v profile is, for all practical purposes, uniform and having an overall magnitude near zero. At higher reduced frequencies, the profile becomes non-zero, with a maximum value occurring at the same height as the maximum in u_{avg} . The average- v velocity, however, is negative over the majority of the profile.

Considering the u_{rms} and v_{rms} profiles, unlike the uniform flow case, a clear asymmetry is seen for all frequencies, except at $k = 6.0$ when the wake is nearly neutral. Below this frequency, there is a distortion in the profiles about $y/c = 0.0$, but the profiles persist near the wake centerline. In contrast, at the higher frequencies of $k = 8.0$ and 11.9 , the asymmetry takes the form of an upwards shift in the profiles, similar to the average u and v profiles. One notable feature in the u_{rms} profile is the development of a third peak at $k = 8.0$, which is barely observable for the uniform flow case. This middle peak exceeds the other two peaks in magnitude at $k = 11.9$.

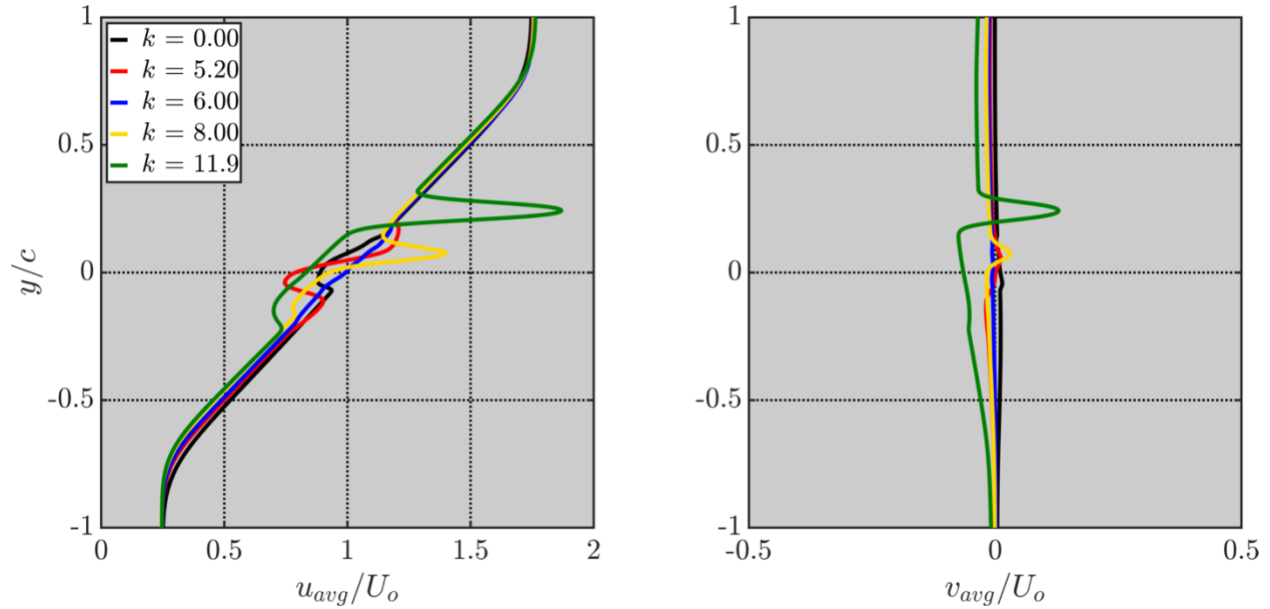


Figure 10. Cross-stream profiles of the average streamwise and cross-stream velocity, extracted at $x/c = 1.0$ for different values of reduced frequency at the highest shear rate considered ($\dot{\gamma} = 1.0$).

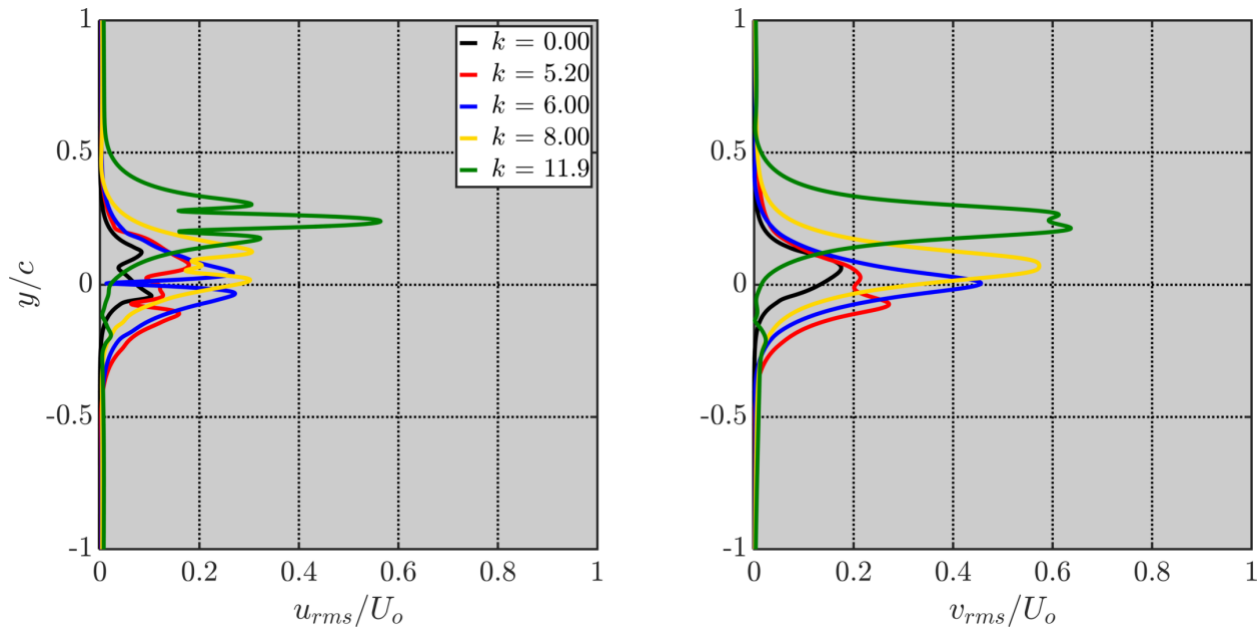


Figure 11. Cross-stream profiles of the *rms* streamwise and cross-stream velocity, extracted at $x/c = 1.0$ for different values of reduced frequency at the highest shear rate considered ($\dot{\gamma} = 1.0$).

The wake structure is visualized in Fig. 12 using instantaneous spanwise vorticity (ω_z) fields for the uniform and the shear ($\dot{\gamma} = 1.0$) flow, side by side. As seen in Fig. 7, the steady airfoil in uniform flow produces a von Kármán vortex street, while the wake structure for the shear case has asymmetry, with the stronger vorticity having the same sign as the vorticity produced by the approach shear flow. At $k = 5.2$, the uniform flow case also produces a von Kármán vortex street, with more well-defined vortices and connecting braids than in the steady airfoil case. The shear case at this value of k shows a much more distorted structure but with the wake configuration remaining in the traditional von Kármán street formation by the end of the domain. During the early evolution of the wake (in the domain stretching to around $X/c = 2.5$), a secondary negative vortex is seen to form and pair with the primary negative vortex. At $k = 6.0$, the vortices are nearly aligned with the wake centerline for *both* the uniform and shear flow cases. This interesting similarity in the formation of the neutral wake is consistent with the observations made earlier based on the wake velocity profiles. At $k = 8.0$ and 11.9 , the vortices in the uniform flow case take on the reverse von Kármán vortex street pattern. In shear, the vortices are also in a reverse von Kármán vortex street configuration (in the sense that the positive vortex is located above the negative one), but the pattern deflects upward towards the high-speed-side. The pair of opposite-sign vortices shed during the same pitching cycle at these two reduced frequencies become isolated and self-propel upward. As the pair of vortices deflect up, vorticity “bleeds” off the negative vortex along the same path followed by the negative vortex. At $k = 11.9$, the vortices are also seen to turn back towards the wake centerline. The angle of wake deflection visually increases as k increases, commensurate with the upwards shift in the jet-like flow and the *rms* velocity profiles observed for $k = 8.0$ and 11.9 . Shear in the approach flow influencing the wake structure deflection was also observed in reference [31] but at a much lower Reynolds number of 3.0×10^3 .

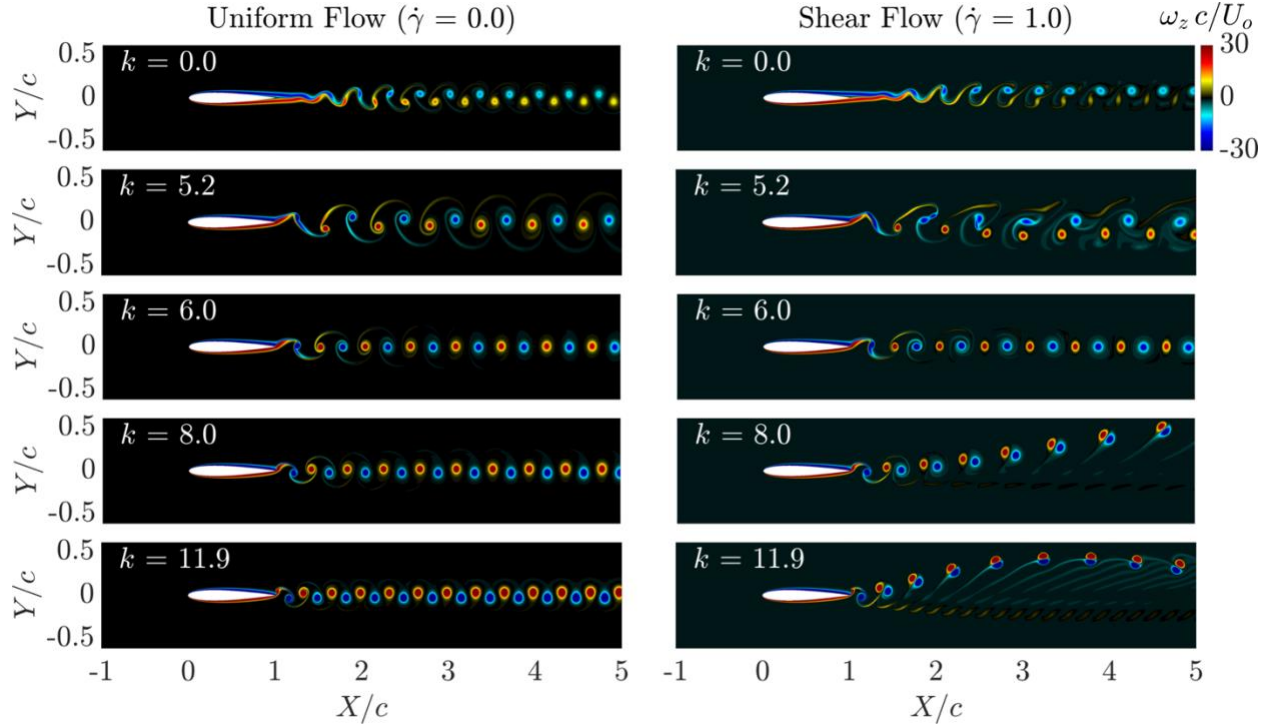


Figure 12. Instantaneous spanwise vorticity fields for $\dot{\gamma} = 0.0$ (left) and 1.0 (right), with increasing reduced frequency from top to bottom. The airfoil is at zero angle of attack and is pitching up.

2. Forces

Figure 13 depicts computational results showing the effect of the reduced frequency on the average lift coefficient, C_L , average thrust coefficient, C_T , peak-to-peak lift-fluctuation coefficient, $C_{L,pp}$, and peak-to-peak thrust-fluctuation coefficient, $C_{T,pp}$, for different shear rates. As expected, for the uniform flow case, the average lift coefficient is zero across the entire range of k . The average thrust coefficient begins at negative values (i.e., drag force), decreases in magnitude as k increases, switches sign to become positive, and then increases in magnitude. This trend, which is well-established in the literature, reflects the switch of the mean streamwise force from drag to thrust with increasing reduced frequency. The lift and thrust fluctuation amplitudes increase as k increases.

In the case of shear, the most obvious difference from uniform flow occurs for the average lift coefficient. At low reduced frequency ($k \leq 1.5$), the lift remains negative and does not change greatly in magnitude from its value at $k = 0.0$. As the reduced frequency increases further, the average lift switches sign to become positive at $k \approx 3.0$ and continues to monotonically increase in magnitude as the reduced frequency increases. Once positive, the average lift increases substantially in magnitude as $\dot{\gamma}$ increases, demonstrating a significant influence of shear on the mean lift. It is noteworthy that the generation of non-zero lift does not coincide with the development of a deflected wake (refer to Fig. 12). Moreover, for cases where the wake does deflect, the sign of the lift is contrary to the expected sign based on the wake deflection in the positive y -direction (i.e., high-speed side). These observations are consistent with behavior seen in the case of deflected wakes in uniform flow, where the connection between deflection direction and sign of lift is counter-intuitive; specifically, that the wake deflection is in the same direction as the lift force (e.g., [32]).

In contrast, the average thrust shows no effect due to shear at frequencies below the switch over frequency (where the streamwise force switches from drag to thrust). At higher frequency, a small effect is seen where increasing $\dot{\gamma}$ augments the thrust coefficient slightly. The independence of the switchover frequency of $\dot{\gamma}$ is consistent with the establishment of the neutral wake for both the uniform and the shear flow at the same reduced frequency; seen earlier from the velocity profiles and vorticity fields (although the thrust switchover frequency is known to be higher than that for the establishment of the neutral wake). The observed behavior in lift and thrust are consistent with the observations in [31], where the lift increases at a given k as the shear rate increases and the thrust is not significantly impacted by shear. These observations were made at a chord Reynolds number of 3.0×10^3 , which is much lower than the present study. Figure 13 also shows that the lift fluctuation amplitude is uninfluenced by shear, while the thrust fluctuation amplitude weakly increases with $\dot{\gamma}$.

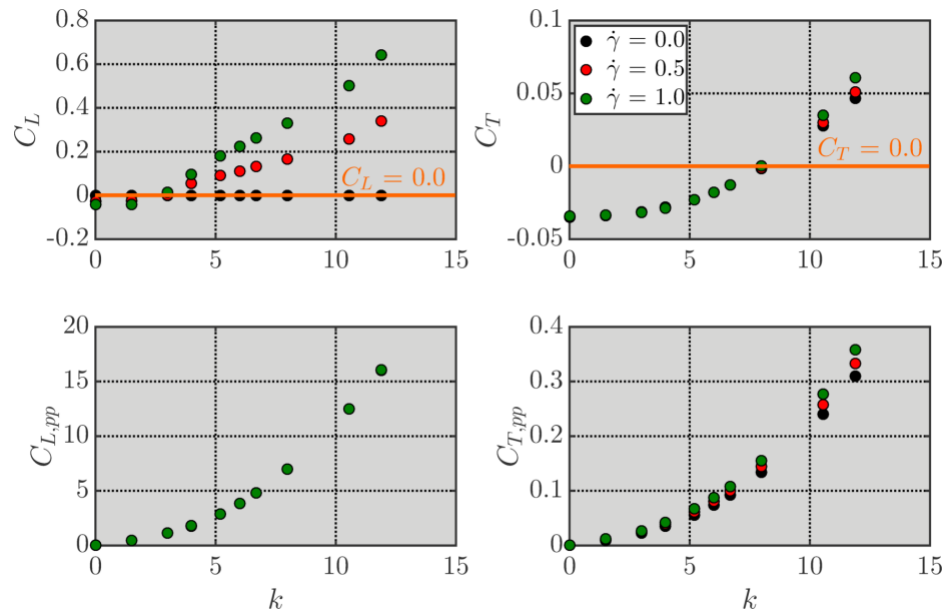


Figure 13. C_L , C_T , $C_{L,pp}$, $C_{T,pp}$ vs. k for different $\dot{\gamma}$ values from the CFD using the three-segment velocity profile. The solid orange lines represent $C_L = 0.0$ and $C_T = 0.0$ in the plots on top.

Experimental observations of lift and thrust are commensurate with the CFD results. The average and peak-to-peak fluctuation of lift and thrust obtained from force measurements are shown in Fig. 14. For comparison, the figure also contains CFD results based on the specific approach velocity profile of the experiments (Fig. 5). Overall, the behavior of the force coefficients in Fig. 14 is very similar that based on Fig. 13 (employing the idealized three-segment approach stream profile). More importantly, the experimental data not only show qualitative but also *quantitative* agreement with the computations (with the exception of some discrepancy in the peak-to-peak values of C_T).

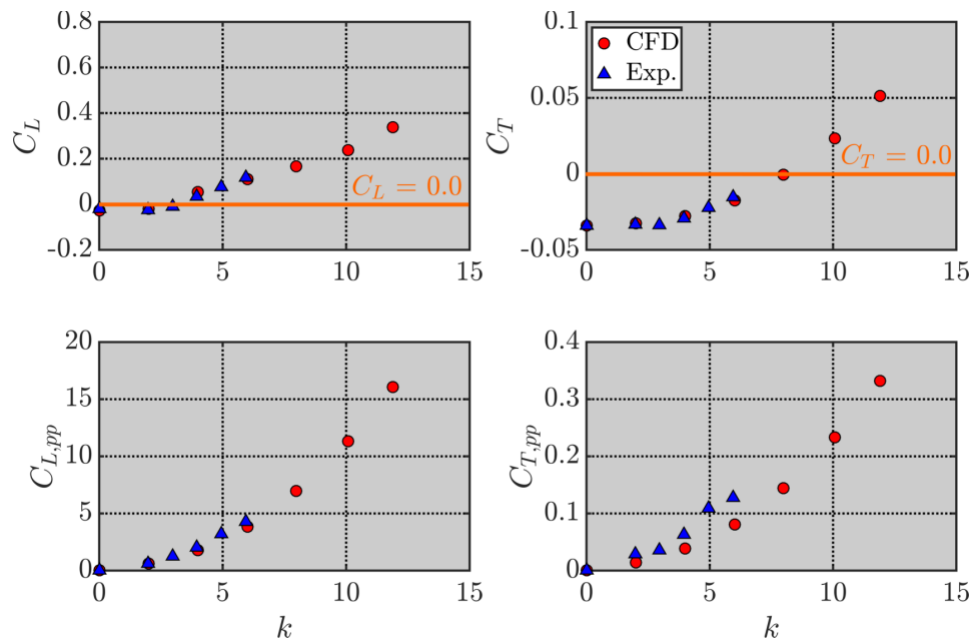


Figure 14. C_L , C_T , $C_{L,pp}$, $C_{T,pp}$ vs. k from the experiments compared to counterpart results from CFD based on the actual experimental velocity profile (Fig. 5). The solid orange lines represent $C_L = 0.0$ and $C_T = 0.0$ in the plots on top.

V. Conclusions

This work considers the effect of shear in the approach flow on the loads and wake structure of an oscillating airfoil using complementary two-dimensional Navier-Stokes computations and direct force measurements. The airfoil is a NACA 0012 profile while the flow is at a Reynolds number based on chord of approximately 1.2×10^4 . The airfoil pitches sinusoidally about its quarter-chord with amplitude of 2° and reduced frequencies k between 0 and approximately 12. The shear approach flow considered in this work is a three-segment profile with linear velocity variation over width δ . The non-dimensional shear rate in the computations varies from 0.0 to 1.0. The non-dimensional shear rate in the experiments is 0.48, which is created using a variable-length honeycomb technique. The width of the shear zone, which is 1.5 times the airfoil chord c in the computations and approximately $2c$ in the experiments, is kept at a large enough value in order to have no effect on the results.

The presence of shear is found to break the symmetry of the wake structure independent of the reduced frequency, and to lead to wake deflection towards the high-speed side at high enough reduced frequencies. Interestingly, the wake vortex street is aligned along the centerline (i.e., neutral wake condition) at $k = 6.0$ for *both* uniform *and* shear flow cases. Below this reduced frequency, the average streamwise velocity profile for both uniform and shear flows predominantly exhibits a velocity defect, or wake. On the other hand, for $k > 6.0$, a velocity surplus, or jet flow, is formed in the wake.

Considering the loads on the airfoil, shear in the approach flow has the most prominent impact on the average lift. At $k \leq 1.5$, the average lift coefficient has a small negative value and it does not change with increasing reduced frequency. The lift coefficient decreases in magnitude at $k > 1.5$ until it switches sign at $k \approx 3.0$, and increases in magnitude monotonically with reduced frequency for a given shear rate. At a given reduced frequency, the magnitude of the lift coefficient increases with the non-dimensional shear rate. In contrast, little or no effect of shear is found on the average thrust coefficient and the peak-to-peak magnitude of the fluctuating thrust and lift. These conclusions are supported by both the computational and experimental results.

Acknowledgments

The authors thank Mitch Albrecht for his assistance with some of the experiments. The first author thanks Daniel Garmann, Caleb Barnes, and Scott Sherer for their technical support using FDL3DI. This work is supported by the Air Force Office of Scientific Research (AFOSR) grant number FA9550-15-1-0224. The views and conclusions contained in this document are those of the authors and should not be interpreted as representing the official policies, either expressed or implied, of AFOSR or the U.S. Government. The U.S. Government is authorized to reproduce and distribute reprints for Government purposes notwithstanding any copyright notation herein.

References

- ¹Koochesfahani, M. M., "Vortical Patterns in the Wake of an Oscillating Airfoil," *AIAA Journal*, Vol. 27, No. 9, 1989, pp. 1200-1205.
- ²Stanek, M. J. and Visbal, M. R., "Study of the Vortical Wake Patterns of an Oscillating Airfoil" *AIAA Paper No. AIAA-89-0554*, 27th Aerospace Sciences Meeting, 9 – 12 January, 1989, Reno, NV.
- ³Anderson, J. M., Streitlien, K., Barrett, D. S., and Triantafyllou, M. S., "Oscillating Foils of High Propulsive Efficiency," *Journal of Fluid Mechanics*, Vol. 360, 1998, pp. 41-72.
- ⁴Lai, J. C. S. and Platzer, M. F., "Jet Characteristics of a Plunging Airfoil," *AIAA Journal*, Vol. 37, No. 12, 1999, pp. 1529-1537.
- ⁵Ramamurti, R. and Sandberg, W., "Simulation of Flow about Flapping Airfoils using Finite Element Incompressible Flow Solver," *AIAA Journal*, Vol. 39, No. 2, 2000, pp. 253-260.
- ⁶Young, J. and Lai, J. C. S., "Oscillation Frequency and Amplitude Effects on the Wake of a Plunging Airfoil," *AIAA Journal*, Vol. 42, No. 10, 2004, pp. 2042-2052.
- ⁷Shyy, W., Lian, Y., Tang, J., Liu, H., Trizila, P., Stanford, B., Bernal, L., Cesnik, C., Friedmann, P., and Ifju, P., "Computational Aerodynamics of Low Reynolds Number Plunging, Pitching and Flexible Wings for MAV Applications," *AIAA Paper No. 2008-523*, 46th AIAA Aerospace Sciences Meeting including the New Horizons Forum and Aerospace Exposition, 7 – 10 January 2010, Reno, NV.
- ⁸Bohl, D. G. and Koochesfahani, M. M., "MTV Measurements of the Vortical Field in the Wake of an Airfoil Pitching at High Reduced Frequency," *Journal of Fluid Mechanics*, Vol. 620, 2009, pp. 63-88.

- ⁹Yu, M.L., Hu, H., and Wang, Z. J., "A Numerical Study of Vortex-Dominated Flow around an Oscillating Airfoil with High-Order Spectral Difference Method," *AIAA Paper No. 2010-726*, 48th AIAA Aerospace Sciences Meeting including the New Horizons Forum and Aerospace Exposition, 4 – 7 January 2010, Orlando, FL.
- ¹⁰Gaitonde, D. V. and Visbal, M. R., "High-Order Schemes for Navier-Stokes Equations: Algorithm and Implementation into FDL3DI," Air Force Research Laboratory AFRL-VA-WP-TR-1998-3060, Wright-Patterson Air Force Base, Ohio, 1998.
- ¹¹Visbal, M. R. and Gaitonde, D. V., "High-Order-Accurate Methods for Complex Unsteady Subsonic Flows," *AIAA Journal*, Vol. 37, No. 10, 1999, pp. 1231-1239.
- ¹²Tannehill, J. C., Anderson, D. A., and Pletcher, R. H., *Computational Fluid Mechanics and Heat Transfer*, McGraw-Hill Book Company, 1997.
- ¹³Beam, R. M. and Warming, R. F., "An Implicit Factored Scheme for the compressible Navier-Stokes Equations," *AIAA Journal*, Vol. 16, No. 4, 1978, pp. 393-402.
- ¹⁴Pulliam, T. H. and Chaussee, D. S., "A Diagonal Form of an Implicit Approximate-Factorization Algorithm," *Journal of Computational Physics*, Vol. 39, No. 2, 1981, pp. 347-363.
- ¹⁵Jameson, A., Schmidt, W., and Turkel, E., "Numerical Solutions of the Euler Equations by Finite Volume Methods using Ruge-Kutta Time Stepping Schemes," *AIAA Paper No. 1981-1259*, AIAA, 1981.
- ¹⁶Pulliam, T., "Artificial Dissipation Models for the Euler Equations," *AIAA Journal*, Vol. 24, No. 12, 1986, pp. 1931–1940.
- ¹⁷Lele, S. K., "Compact Finite Difference Schemes with Spectral-like Resolution," *Journal of Computational Physics*, Vol. 103, 1992, pp. 16-42.
- ¹⁸Hammer, P. R., "Computational Study on the Effect of Reynolds Number and Motion Trajectory Asymmetry on the Aerodynamics of a Pitching Airfoil at Low Reynolds Number," PhD. Dissertation, Mechanical Engineering Department, Michigan State University, East Lansing, MI, 2016.
- ¹⁹Suhs, N. E., Rogers, S. E., and Dietz, W. E., "Pegasus 5: An Automated Pre-Processor for Overset-Grid CFD," *AIAA Paper No. 2002-3186*, 32nd AIAA Fluid Mechanics Conference, AIAA Aviation, 24 – 26 June, 2002, St. Louis, MO.
- ²⁰Visbal, M. R. and Gaitonde, D. V., "Very High-Order Spatially Implicit Schemes for Computational Acoustics on Curvilinear Meshes," *Journal of Computational Acoustics*, Vol. 9, No. 4, 2001, pp. 1259-1286.
- ²¹Sherer, S. E. and Scott, J. N., "High-Order Compact Finite-Difference Methods on General Overset Grids," *Journal of Computational Physics*, Vol. 210, 2005, pp. 459-496.
- ²²Sherer, S. E. and Visbal, M. R., "Multi-Resolution Implicit Large Eddy Simulation using a High-Order Overset Grid Approach," *International Journal of Numerical Methods in Fluids*, Vol. 55, 2007, pp. 455-482.
- ²³Morton, S. A., Melville, R. B., and Visbal, M. R., "Accuracy and Coupling Issues of Aeroelastic Navier-Stokes Solutions on Deforming Meshes," *Journal of Aircraft*, Vol. 35, No. 5, 1998, pp. 798-805.
- ²⁴Visbal, M. R. and Gaitonde, D. V., "On the Use of Higher-Order Finite-Difference Schemes on Curvilinear and Deforming Meshes," *Journal of Computational Physics*, Vol. 181, 2002, pp. 155-185.
- ²⁵Persson, P.-O., Bonet, J., and Peraire, J., "Discontinuous Galerkin Solution of the Navier-Stokes Equations on Deformable Domains," *Computers and Fluids*, Vol. 198, 2009, pp. 1585-1595.
- ²⁶Kotansky, D.R., "The Use of Honeycomb Shear Flow Generation," *AIAA Journal*, Vol 4, No. 8, 1966, pp. 1490-1491.
- ²⁷Safaripour, A., Olson, D., Naguib, A., and Koochesfahani, M., "On Using Shaped Honeycombs for Experimental Generation of Arbitrary Velocity Profiles in Test Facilities," *Bulletin of American Physical Society*, Vol. 61, No. 20, 2016, p. 265.
- ²⁸Tsien, H., "Symmetrical Joukowski Airfoils in Shear Flow," *Quarterly of Applied Mathematics*, Vol. 1, No. 2, 1943, pp. 130-148.
- ²⁹Hammer, P. R., Visbal, M. R., Naguib, A. M., and Koochesfahani, M. M., "Lift on a Steady 2-D Symmetric Airfoil in a Viscous Uniform Shear Flow," *Journal of Fluid Mechanics*, Vol. 837, R2, 2018 (<https://doi.org/10.1017/jfm.2017.895>).
- ³⁰Naguib, A. M., Vitek, J., and Koochesfahani, M. M., "Finite-Core Vortex Array Model of the Wake of a Periodically Pitching Airfoil," *AIAA Journal*, Vol. 49, No. 7, 2011, pp. 1542-1550.
- ³¹Yu, M., Wang, B., Wang, Z. J., and Farokhi, S., "Evolution of Vortex Structures over Flapping Foils in Shear Flow and its Impact on Aerodynamic Performance," *Journal of Fluids and Structures*, Vol. 75, 2018, pp. 116-134.
- ³²Cleaver, D. J., Wang, Z. J., and Gursul, I., "Bifurcating Flows of Plunging Aerofoils at High Strouhal Numbers," *Journal of Fluid Mechanics*, Vol. 708, 2012, pp. 349-376.